metals

MDPI

Article

Influence of CeO_2 Addition on Microstructure and Wear Behavior of Plasma Spray-Welded Stellite6/WC Composite Coatings

Meiqiao Wu, Zhengbing Meng *, Yajie Cui, Rongxin Lan, Jiangbo Deng, Dinghua Feng and Zixun He

College of Materials Science and Engineering, Guilin University of Technology, Guilin 541004, China; wumeiqiao2023@163.com (M.W.); cuiyj0805@163.com (Y.C.); 18185991109@163.com (R.L.); 15886680080@163.com (J.D.); lh17459200@163.com (D.F.); hezixun318@163.com (Z.H.)

* Correspondence: mengzbing@163.com

Abstract

This study systematically investigates the influence of CeO_2 content (0–0.6 wt.%) on the microstructure and mechanical properties of Stellite6/WC composite coatings fabricated by plasma spray welding. The phase composition and microstructure of the coatings were characterized using X-ray diffraction (XRD) and scanning electron microscopy (SEM), while microhardness and tribological performance were evaluated using a semi-automatic Vickers microhardness tester and a ball-on-disk tribometer. The results indicate that the coating with 0.4 wt.% CeO_2 exhibits the optimal combination of mechanical and tribological properties, achieving a maximum microhardness of 1107.62 $HV_{0.3}$—a 50.5% improvement over the unmodified coating—and a minimum wear mass loss of 1.4 mg, corresponding to a 78.1% reduction compared to the CeO_2-free counterpart. These findings demonstrate that appropriate CeO_2 addition significantly enhances both the microhardness and wear resistance of Stellite6/WC coatings, offering an effective strategy to mitigate surface degradation and extend the service life of 45 steel substrates under demanding operating conditions.

Keywords: plasma spray; CeO_2; Stellite6/WC; wear

1. Introduction

45 steel, a medium-carbon structural steel, is extensively utilized in the manufacturing of critical transmission components such as gears, shafts, and bearings, owing to its favorable strength-to-toughness ratio and machinability [1,2]. In these applications, components are routinely subjected to sliding and rolling contact, making surface degradation due to wear a primary failure mechanism. However, the inherently low hardness and limited wear resistance of 45 steel render it susceptible to surface damage under demanding tribological conditions, thereby limiting its service life [3]. Surface modification techniques provide an effective strategy to enhance surface durability and extend the lifespan of such components [4].

Among various surface engineering methods, plasma spray welding has emerged as a promising technique for depositing wear-resistant coatings due to its high deposition rate, relatively low heat input to the substrate, cost-effectiveness, and ability to produce thick, metallurgically bonded coatings. Cobalt-based alloys, particularly Stellite6, are frequently employed as coating matrices owing to their excellent high-temperature stability, toughness, and adhesive wear resistance, which arise from a combination of a tough Co-based solid solution and hard phases such as chromium carbides and intermetallic compounds [5–7].

Check for updates

Academic Editor: Francesca Borgioli

Received: 8 March 2026
Revised: 7 April 2026
Accepted: 8 April 2026
Published: 10 April 2026

Copyright: © 2026 by the authors. Licensee MDPI, Basel, Switzerland. This article is an open access article distributed under the terms and conditions of the Creative Commons Attribution (CC BY) license.

To further enhance wear resistance for severe applications, ceramic reinforcements like WC are commonly incorporated. WC particles act as the primary load-bearing phase, and their partial decomposition during the high-temperature process leads to the formation of secondary hard phases—including W_2C, Co_6W_6C, and Fe_6W_6C—that contribute to increased hardness and wear resistance [8–10]. However, the direct addition of such reinforcement particles presents challenges. For instance, Zhang et al. [11] and Zheng et al. [12] observed that adding WC coatings can improve hardness and wear resistance, but they also noted issues such as particle aggregation, poor interfacial bonding, and a tendency for reinforcement phases to peel off during wear, which can compromise coating integrity and long-term performance.

Rare earth (RE) elements and their oxides have attracted considerable attention as microalloying additives in surface engineering due to their unique ability to refine microstructure and optimize properties, even when added in trace amounts [13]. RE elements are known to segregate at grain boundaries, scavenge impurities, modify the type, morphology, and distribution of precipitated phases, and improve oxidation and corrosion resistance [14–16]. In the context of wear-resistant coatings, RE oxides like CeO_2 are not merely inert additional reinforcements [17,18]. Instead, they function as active modifiers, influencing the molten pool's behavior and the subsequent solidification process. Studies have shown that the addition of rare earth elements has a significant effect on the overall performance of the alloy. Usually, their additions are controlled between 0.05% and 4%. When the rare earth content is lower than 0.1%, it has little effect on the enhancement of cemented carbide performance [14]. When the dosage reaches the range of 0.3% to 0.8% [19], it can significantly improve the comprehensive performance of cemented carbide; however, once the content exceeds 1.5% [20], the rare earth enrichment phenomenon occurs within the tungsten carbide, which weakens the optimization of the performance of rare earth elements. If the rare earth content exceeds 4%, it will lead to a decrease in the strength of cemented carbide [21], at which time the rare earth element has been transformed into an impurity. Therefore, when using rare earth additions to optimize the performance of cemented carbide, it is crucial to precisely control the optimal dosage. For example, Pu et al. [22] demonstrated that adding 0.2 wt.% CeO_2 to a Ni-based WC coating deposited by plasma spray welding refined the microstructure, eliminated pores and cracks, and significantly increased hardness and wear resistance. This improvement was attributed to the role of CeO_2 in refining the matrix structure and promoting a more uniform distribution of the WC phase.

The novelty of this work resides in its focus on the regulatory role of CeO_2 on the WC's dissolution–precipitation kinetics within the Stellite6/WC system under plasma spray welding conditions. By carefully controlling the CeO_2 content, this study aims to reveal how it governs the diffusion of W and C, the formation and distribution of secondary hard phases, and the resulting tribological performance. Therefore, this study fabricates CeO_2-modified WC/Stellite6 composite coatings on 45 steel substrates via optimized plasma spray welding. It systematically investigates the influence of varying CeO_2 additions (0 to 0.6 wt.%) on the coating's phase constituents, microstructural characteristics, microhardness, and wear resistance. The work aims to establish a coherent link between the CeO_2 content, the resulting microstructural mechanisms, and the final mechanical/tribological properties, thereby providing a scientific basis for designing durable, high-performance protective coatings.

2. Experiments and Materials

2.1. Preparation of Plasma Cladded Coatings

The 45 steel (100 mm × 50 mm × 10 mm) was selected as the substrate in this study. Its chemical composition, as provided by the supplier and listed in Table 1, was determined

by professional spectrometry analysis. All substrates were mechanically ground with sandpaper to remove the surface oxide layer, and then ultrasonically cleaned successively with acetone and ethanol to eliminate oil and impurities. To alleviate thermal stress, the substrates were preheated in an oven prior to the plasma spray welding process.

Table 1. Chemical composition of substrates (wt.%).

Element (wt.%)	C	Cr	Mn	Ni	P	S	Si	Fe
45 steel	0.43	≤0.25	0.50	≤0.25	≤0.35	≤0.35	0.17	Bal.

The composite coatings were fabricated using a mechanically blended feedstock powder consisting of three components: Stellite6 alloy, WC, and CeO_2. Spherical Stellite6 powder (100–325 mesh) functioned as the metallic binder matrix, with its chemical composition—determined by the supplier via professional spectroscopic analysis—provided in Table 2. The morphology of each powder is presented in Figure 1. Subsequently, the Stellite6, WC, and CeO_2 powders were uniformly blended via ball milling under a weight ratio of 5:1 (balls to powder), a rotational speed of 200 rpm, and a duration of 1 h.

Table 2. Chemical composition (wt.%) of Stellite6 self-fusing alloy powder.

Element (wt.%)	Cr	Si	Fe	Ni	W	C	Co
Stellite6	31.66	1.10	3.00	2.24	4.64	1.15	Bal.

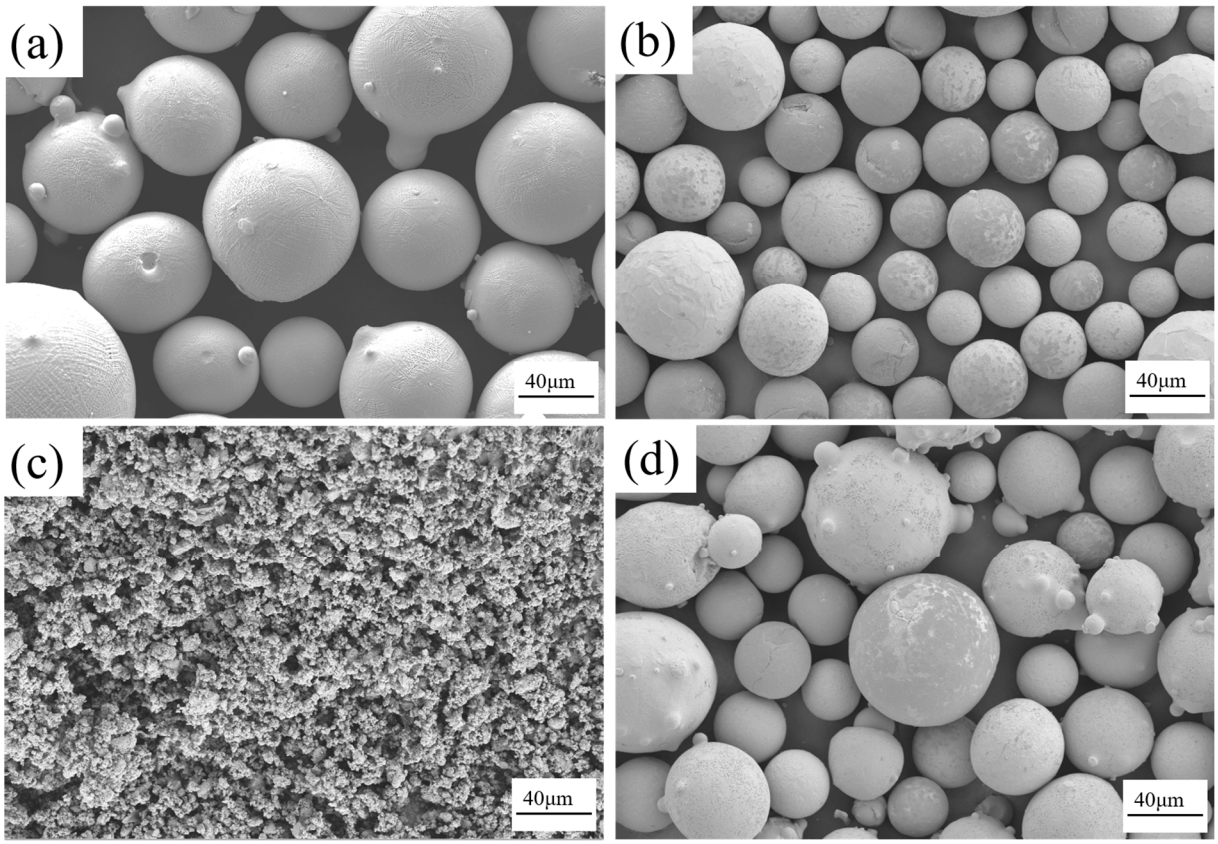


Figure 1. Morphology for powders of (**a**) Stellite6; (**b**) WC; (**c**) CeO_2; (**d**) Stellite6 + 40% WC + 0.4% CeO_2.

Coating deposition was performed using a CNC multi-function powder plasma spraying system (DML-V03BD, Shanghai Dolmu Industry Co., Shanghai, China). This process

utilizes a high-energy plasma arc to instantaneously melt the feedstock powder and project it onto the substrate surface. To investigate the influence of CeO_2 addition on the coating's microstructure and properties, four distinct powder blends with varying CeO_2 contents (see Table 3 for details) were prepared.

Table 3. Compositional design of different composite coatings (wt.%).

No.	Commercial Stellite6 Powder	WC Powder	CeO_2 Powder
C0	60	40	0
C1	59.8	40	0.2
C2	59.6	40	0.4
C3	59.4	40	0.6

Through preliminary optimization tests, the following process parameters were established and maintained for all depositions: a spraying current of 140–170 A, a plasma gas flow rate of 4.5 L/min, a powder feed rate of 30–40 g/min, a torch traverse speed of 80 mm/s, and a stand-off distance of 5 cm between the nozzle and the substrate surface.

2.2. Characterization of Plasma Cladded Coatings

For microstructural and compositional characterization, metallographic specimens (10 mm × 10 mm × 5 mm) were sectioned perpendicular to the spraying direction. The cross-sectional surfaces were ground progressively using sandpapers from 180# to 2000# grit and then polished to a mirror finish. To reveal the microstructure, the polished samples were etched with diluted aqua regia (50 vol% HNO_3 + 25 vol% HCl + 25 vol% H_2O) for 10–15 s. Microstructural features and elemental distribution of the coatings were examined using a Gemini SEM 300 scanning electron microscope (ZEISS, Oberkochen, Germany) equipped with an energy dispersive X-ray spectrometer (EDS). Phase identification was carried out by X-ray diffraction (XRD) with Cu Kα radiation at room temperature (25 °C), employing a scanning speed of 10°/min and a step size of 0.02°; this parameter set was chosen to ensure adequate diffraction peak resolution for qualitative phase analysis while maintaining reasonable data acquisition efficiency. Furthermore, microhardness measurements were performed on the coating cross sections using a semi-automatic Vickers hardness tester (model EV 4000TK, QATM, Mammelzen, Germany) under a load of 0.3 Kgf with a dwell time of 10 s. To ensure statistical reliability, approximately 14 indentations were made for each coating.

The samples were cut into sizes of 20 mm × 20 mm × 5 mm, and friction wear tests were carried out on samples with different CeO_2 contents using a UMT-2 tribometer (Bruker, Billerica, MA, USA). The experimental procedure was conducted under a load of 50 N, with a rotational motion radius of 8 mm, a friction rate of 200 r/min, and a duration of 1 h. Silicon nitride ceramic spheres with a diameter of 6 mm were used as the friction surface. Three samples were selected for testing in each group, and the average value was taken to eliminate the effect of random error to obtain the wear quality loss. At the end of the wear test, the wear morphology of the coatings was observed using a white light interferometer and a scanning electron microscope.

3. Results and Discussion

3.1. Phase Composition and Elemental Distribution

The phase composition of the coatings was analyzed by X-ray diffraction (XRD) to elucidate the influence of CeO_2 addition on phase formation and stability. It should be noted that, for clarity in the diffraction patterns presented in Figure 2, not all identified phases are labeled with their corresponding ICDD PDF card numbers in each individual

pattern, especially when the same phase appears across multiple spectra; the primary focus is placed on indicating the characteristic peaks of newly formed or significantly altered phases. The introduction of CeO_2 markedly modifies the phase evolution of the coatings. As shown in Figure 2a), the XRD pattern of the coating without CeO_2 addition reveals a phase composition primarily consisting of a Cr–Fe–Ni solid solution matrix, along with W_2C, $Cr_{23}C_6$, and $(Cr, Fe)_7C_3$ type carbides. The presence of W_2C is attributed to the partial decarburization of the original WC particles under the high-temperature plasma arc, whereas the chromium-rich carbides ($Cr_{23}C_6$ and $(Cr, Fe)_7C_3$) precipitate directly from the melt during solidification, owing to the substantial carbon and chromium content of the Stellite6 matrix. Notably, distinct diffraction peaks corresponding to the original WC phase are not clearly discernible, which likely results from its preferential settling toward the lower region of the coating during deposition. Consequently, given the relatively limited fraction of secondary carbide precipitates, solid solution strengthening remains the dominant strengthening mechanism in this coating.

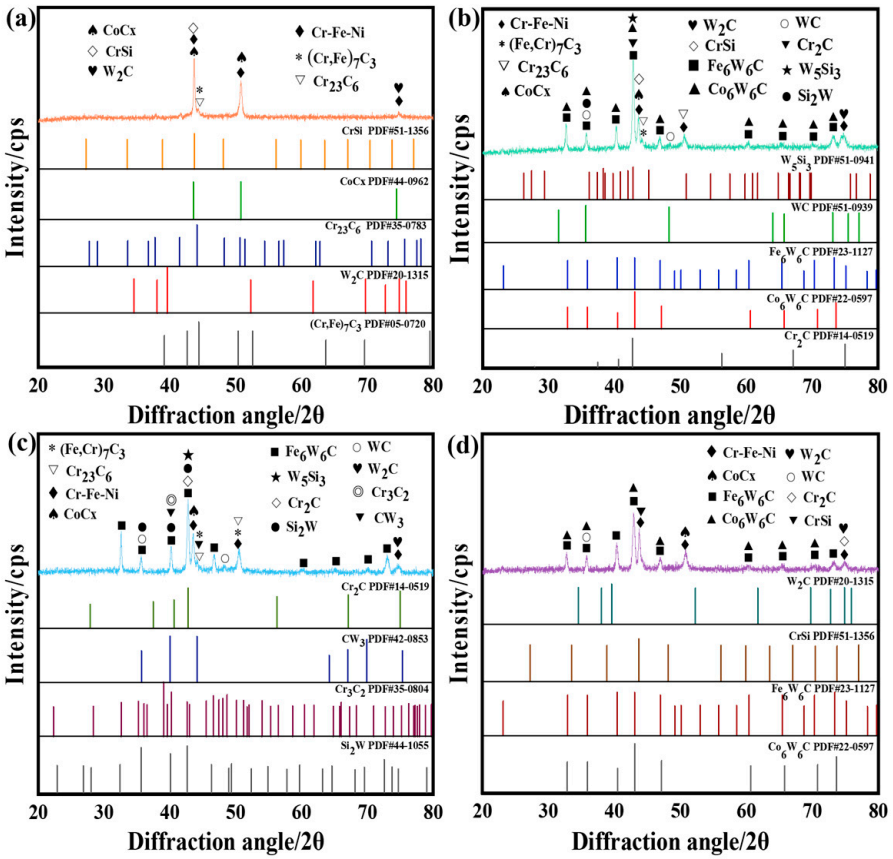


Figure 2. Phase identification of different coatings: (**a**) C0:0 wt.% CeO_2; (**b**) C1:0.2 wt.% CeO_2; (**c**) C2:0.4 wt.% CeO_2; (**d**) C3:0.6 wt.% CeO_2.

The introduction of CeO_2 markedly modifies the phase evolution of the coatings. At a CeO_2 content of 0.2 wt.% (Figure 2b), new phases—including η-carbides (Fe_6W_6C, Co_6W_6C) and silicides (CrSi, WSi_2)—are formed, indicating that CeO_2 actively intervenes in solute partitioning and interfacial reactions during solidification [23]. From a thermodynamic perspective, CeO_2, acting as a surface-active element, reduces the solid/liquid interfacial energy, thereby lowering the heterogeneous nucleation barrier for η-carbides and silicides. Furthermore, CeO_2 increases the activity coefficients of W and C in the molten pool, facilitating the formation of these high-melting-point phases at relatively elevated temperatures [24]. The η-carbides, as hard and brittle intermetallic compounds, effectively impede dislocation motion, thereby increasing the microhardness of the coating. The

silicides (CrSi, WSi_2) exhibit high hardness and good thermal stability, further enhancing the load-bearing capacity during sliding contact. Nevertheless, the metastable Co_6W_6C phase possesses limited thermal stability and is susceptible to decomposition under the frictional heat generated during wear.

Upon increasing the CeO_2 content to 0.4 wt.% (Figure 2c), the metastable Co_6W_6C phase completely disappears. This phenomenon is primarily attributed to the segregation of Ce^{3+} ions at grain boundaries, which elevates the chemical potential of Co_6W_6C and renders it thermodynamically unstable. Consequently, the system evolves toward a more stable assemblage, favoring the precipitation of equilibrium η-carbides (Fe_6W_6C) and silicides (CrSi, WSi_2). Moreover, the high oxygen affinity of CeO_2 reduces the local oxygen partial pressure, further stabilizing oxides and complex carbides. Thus, the observed phase transformation is driven by a combination of reduced nucleation barriers, altered solute activities, and destabilization of metastable phases—all induced by the addition of CeO_2. As a result, thermodynamically stable carbides (Cr_3C_2, CW_3) and stable silicides (W_5Si_3, WSi_2) become predominant. The formation of Cr_3C_2 and CW_3 offers several advantages. These carbides possess high hardness and remain thermodynamically stable even at elevated temperatures, making them effective barriers against plastic deformation; the silicides W_5Si_3 and Si_2W, characterized by high melting points and strong covalent bonding, further enhance resistance to abrasive wear. The complete transformation from metastable to stable phases shifts the primary strengthening mechanism from solid-solution strengthening and partial dispersion strengthening to precipitation strengthening via stable carbides and silicides.

When an excessive amount of CeO_2 is added (Figure 2d), its high melting point leads to agglomeration, resulting in localized compositional inhomogeneity. Paradoxically, this hinders the long-range diffusion of Si and W, exacerbates the non-equilibrium decomposition of WC, and may induce the re-emergence of metastable phases (e.g., trace amounts of Co_6W_6C reappear). Consequently, the volume fraction of desirable stable reinforcing phases (Cr_3C_2, CW_3, W_5Si_3, WSi_2) decreases. The agglomerated particles act as stress concentrators and compromise the overall structural integrity of the skeleton network, ultimately diminishing the strengthening effect.

3.2. Microstructure

Figure 3 displays the cross-sectional microstructures of coatings with varying CeO_2 contents, with coating thicknesses ranging from approximately 2 to 3 mm. Pronounced microstructural variations are observed as the CeO_2 content changes.

In the coating without CeO_2 addition (Figure 3(a1)), relatively coarse WC particles are visible near the substrate interface. This feature can be attributed to the incomplete melting and dissolution of WC particles in this region: owing to the high melting point of WC and the steep temperature gradient near the interface, the local residence time above the liquidus is insufficient for complete dissolution of all WC particles, leaving behind partially retained coarse WC agglomerates. In contrast, the middle-to-upper region of the same coating (Figure 3(a2)) exhibits noticeably finer WC particles along with a limited number of distinct pores. The finer particle size in this region results from prolonged melt existence and more complete dissolution of WC, followed by rapid solidification that suppresses particle growth. The presence of pores is likely due to gas entrapment during the turbulent flow of the molten pool, which becomes more pronounced in regions where solidification outpaces bubble escape.

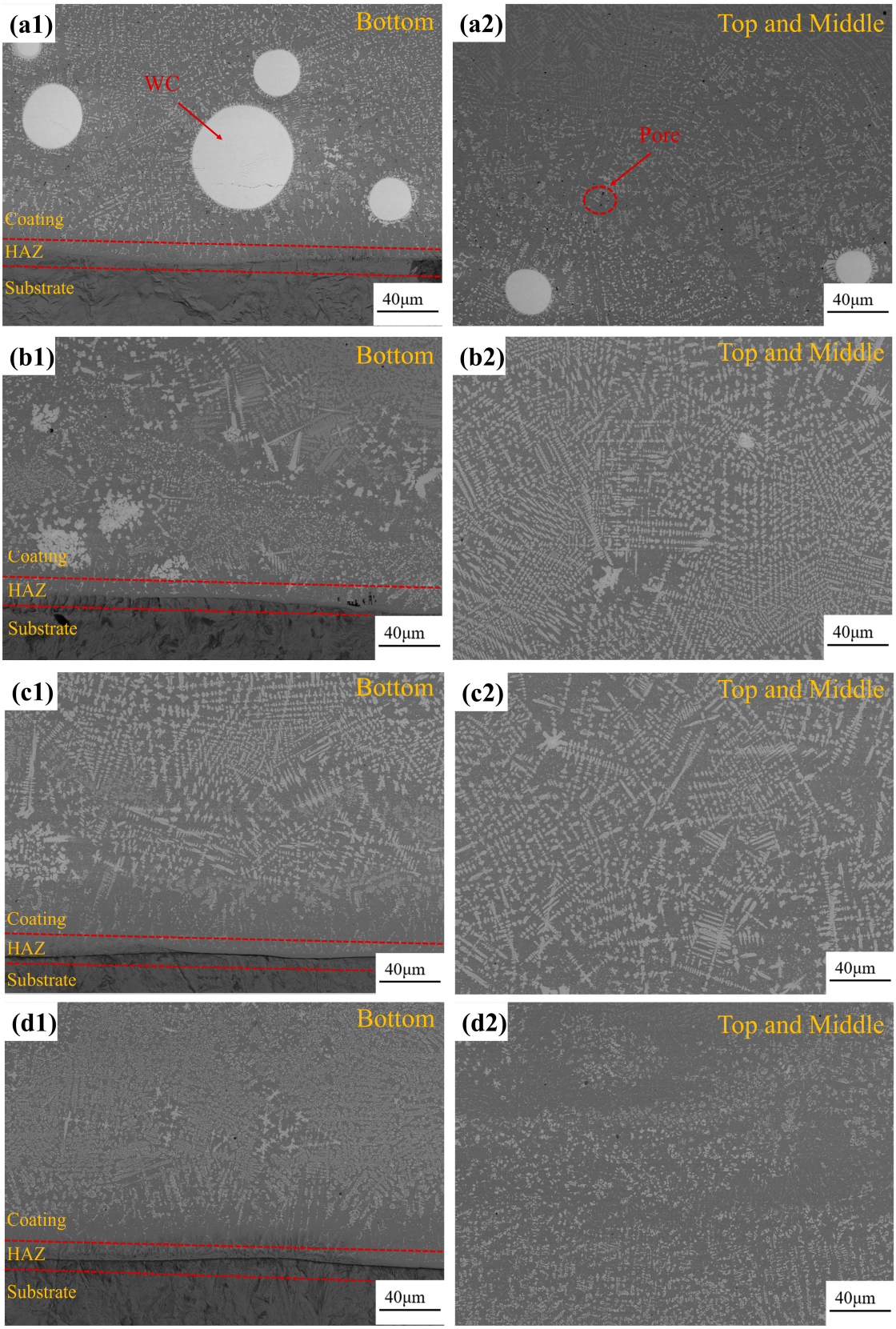


Figure 3. Microstructures of composite coatings with different CeO_2 contents at different locations. (**a1**,**a2**) C0:0 wt.% CeO_2; (**b1**,**b2**) C1:0.2 wt.% CeO_2; (**c1**,**c2**) C2:0.4 wt.% CeO_2; (**d1**,**d2**) C3:0.6 wt.% CeO_2.

In contrast, there is no obvious enrichment of WC particles in the CeO_2-modified weld layer as shown in Figure 3(b1), and there are almost no large WC particles at the bottom of

the solder layer in Figure 3(c1,d1), and there is a distribution of refined W-rich phases in the middle-upper region, as shown in Figure 3(b2,c2). These diffusely distributed W-rich hard phases act as non-deformable second-phase particles, which can directly hinder dislocation slip and effectively improve the mechanical properties of the coatings. This phenomenon stems from the high-density nature of CeO_2, which significantly reduces the melt surface tension and increases the viscosity, and enhances the cobalt matrix's ability to coat the WC particles by optimizing the interfacial wettability of the molten cobalt matrix with the WC particles, which leads to the inhibition of particle agglomeration and the improvement of the uniformity of dispersion [25]. On the one hand, CeO_2 can be used as the substrate for heterogeneous nucleation to reduce nucleation barriers, which induces the formation of equiaxed grains and inhibits the growth of columnar crystals. On the other hand, the ionic radius of Ce^{3+} is much larger than that of Co^{2+}, and it is difficult to solid-solve into the Co matrix lattice, so CeO_2 tends to be enriched at grain boundaries to reduce the total energy of the system [26]. The adsorption of CeO_2 at grain boundaries inhibits the migration of the boundaries and hampers the anomalous grain boundary growth behaviors, which improves the densification of the coatings.

The formation of a three-dimensional hard skeleton network is critical to understanding the wear performance enhancement induced by CeO_2 addition. As shown in Figure 3, the morphology and connectivity of this network exhibit a strong dependence on CeO_2 content [27]. For the coating without CeO_2 addition (Figure 3(a1,a2)), the reinforcing phases—primarily WC particles and a limited number of carbides—are sparsely distributed within the Stellite6 matrix. These phases exist as discrete, isolated particles without forming an interconnected network. Consequently, the load-bearing capacity during friction is limited, as the applied stress is concentrated on the relatively softer matrix, leading to premature material removal. Upon the addition of 0.2 wt.% CeO_2 (Figure 3(b1,b2)), a notable morphological transition occurs. The originally discrete WC particles become partially interconnected through the precipitation of carbides and silicides at particle interfaces. These newly formed phases act as "bridges" that link adjacent hard particles, initiating the formation of a locally interconnected network. However, at this content level, the network remains discontinuous, with some regions still lacking sufficient interconnections. When the CeO_2 content increases to 0.4 wt.% (Figure 3(c1,c2)), a well-developed three-dimensional hard skeleton network is established. The reinforcing phases—including WC particles, carbides, and silicides—form a continuous, interconnected framework that permeates the entire coating. This network exhibits high connectivity, with hard phases uniformly distributed and intimately bonded to the matrix. The formation of such a continuous skeleton is attributed to the catalytic effect of CeO_2, which promotes the synthesis and uniform dispersion of reinforcing phases. Further increasing the CeO_2 content to 0.6 wt.% (Figure 3(d1,d2)) leads to network degradation. Excessive CeO_2 causes over-refinement and agglomeration of reinforcing particles, disrupting the continuity of the skeleton. The originally interconnected framework becomes fragmented, with some regions exhibiting particle clustering and others showing depletion of reinforcing phases. This morphological deterioration negatively impacts the load-bearing capacity of the coating during wear.

Figure 4 presents the quantitative image analysis results of the average grain size of the matrix phase for each coating composition. Figure 5 illustrates the influence of CeO_2 content on the evolutionary behavior of WC particles and the resulting grain size of the coating matrix, with the corresponding microstructures shown in Figure 5a–d.

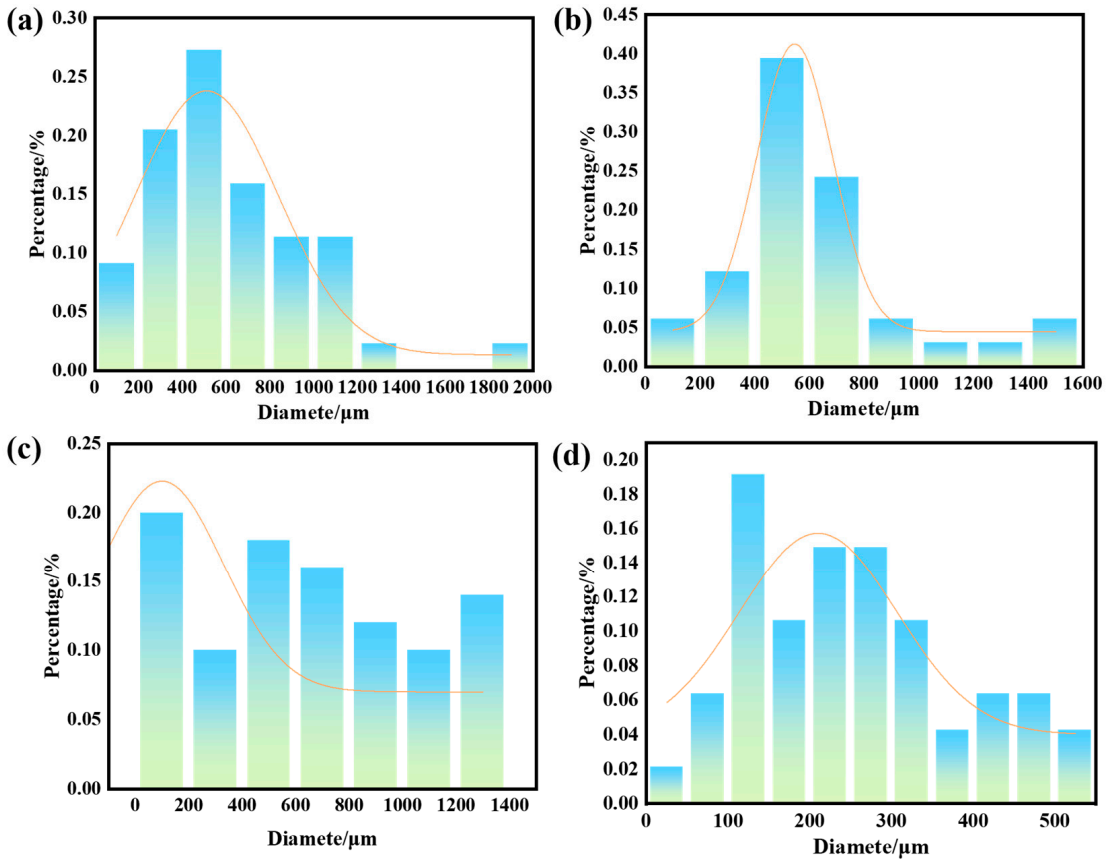


Figure 4. Grain sizes for different CeO_2 contents. (**a**) C0:0 wt.% CeO_2; (**b**) C1:0.2 wt.% CeO_2; (**c**) C2:0.4 wt.% CeO_2; (**d**) C3:0.6 wt.% CeO_2.

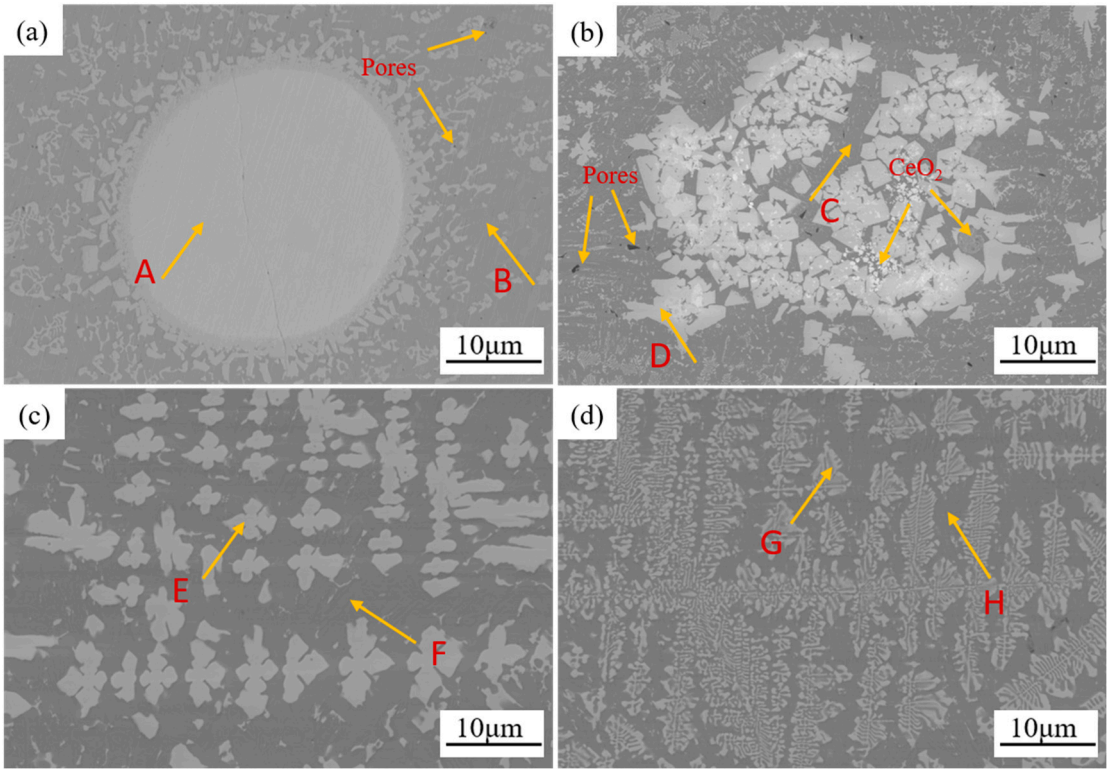


Figure 5. Patterns of different CeO_2 contents on the evolutionary behavior of WC particles (**a**) C0:0 wt.% CeO_2; (**b**) C1:0.2 wt.% CeO_2; (**c**) C2:0.4 wt.% CeO_2; (**d**) C3:0.6 wt.% CeO_2.

For the coating without CeO_2 addition, the WC particles retain a near—spherical morphology, and only localized diffusive dissolution occurs at their edges, indicating that the heat input from the molten pool is insufficient to drive complete decomposition. Accordingly, the matrix exhibits the coarsest grain structure, with an average grain size of 1133.83 μm. This coarse microstructure is attributed to the absence of CeO_2, which otherwise promotes heterogeneous nucleation and grain refinement. Upon the addition of 0.2 wt.% CeO_2, the WC particles show signs of partial decomposition, accompanied by more pronounced solute diffusion at the particle/matrix interface. The average grain size of the matrix decreases significantly to 766.48 μm, representing a reduction of approximately 32.4% compared to C0 [28,29]. This refinement is attributed to the CeO_2—induced enhancement of melt pool activity, which facilitates heterogeneous nucleation and restricts grain growth. When the CeO_2 content is increased to 0.4 wt.%, the WC particles exhibit complete decomposition characteristics, with substantial solute diffusion at the interface. The W and C elements are uniformly distributed in the matrix through liquid—phase migration, as confirmed by XRD analysis. The average grain size further decreases to 630.94 μm, corresponding to reductions of 44.4% relative to C0 and 17.7% relative to C1. This optimal refinement is associated with the formation of a continuous three—dimensional hard skeleton network composed of stable carbides and silicides, which effectively pins grain boundaries and restricts grain growth.

At an excessive CeO_2 content of 0.6 wt.%, despite the near-complete decomposition of WC particles, the average grain size drops dramatically to 236.81 μm, which is the finest among all compositions. This excessive refinement may be attributed to pronounced agglomeration of CeO_2 particles, which serve as numerous heterogeneous nucleation sites, resulting in an extremely high nucleation density. However, this over-refinement is accompanied by CeO_2 agglomeration and local compositional inhomogeneity, which compromise the structural integrity of the skeleton network and ultimately lead to a decrease in hardness and wear resistance. Thus, while the finest grain size is achieved at 0.6 wt.% CeO_2, the optimal balance between grain refinement and microstructural homogeneity is obtained at 0.4 wt.% CeO_2.

This transformation can be attributed to the CeO_2-induced enhancement effect of the melt pool activity. Notably, under the condition of moderate addition of CeO_2 as in Figure 5c, a stable maple-leaf-like structure is formed on the surface of WC particles, which is essentially due to the stabilization of the proportion of W in the solid solution in γ-Co between 18.00~19.59% [30], which restricts the further solid solution of WC and results in the formation of equilibrium phases by recrystallization of the supersaturated W atoms at the WC/Co interface. This maple leaf-shaped structure significantly enhances the interfacial bond strength through the pinning effect. However, as shown in Figure 5d, the introduction of excess CeO_2 leads to the formation of disordered dendritic substructures in WC particles, and this nanoscale dispersed phase exacerbates the interfacial stress concentration due to the surge in specific surface area, which ultimately adversely affects the macroscopic mechanical properties of the coatings.

Table 4 presents the key EDS microanalysis results that directly elucidate the elemental redistribution induced by CeO_2 addition, thereby corroborating the phase evolution identified by XRD. The data clearly differentiate two distinct microstructural constituents: the white phase (points A, D, E, G) is predominantly enriched in W and Co, aligning with the XRD-identified carbides (WC, W_2C, CoC_x). It should be noted that the WC powder used in this study is pure WC without any metallic binder; therefore, the Co detected in the white phase originates from the interdiffusion between WC particles and the surrounding Stellite6 melt during the plasma spray welding process. As a result, the white phase is still referred to as the WC phase due to its partially retained morphology, although its composition

has been modified by the infiltration of Co, Cr, and Fe from the matrix. Conversely, the gray phase (points B, C, F, H) is rich in Co, Cr, and Fe. Crucially, the detection of Si and trace Ce within specific gray phase regions (points C, F, H) provides direct microchemical evidence that CeO_2 incorporation promotes the segregation and subsequent precipitation of Si, leading to the formation of silicides (W_5Si_3, Si_2W) as confirmed by XRD.

Table 4. EDS micro-component analysis.

Element (wt.%)	A	B	C	D	E	F	G	H
C	4.47	3.86	4.71	3.46	3.89	3.32	3.87	4.36
W	67.29	22.03	11.87	69.72	58.23	9.91	51.88	10.36
Co	11.04	25.67	39.25	16.41	17.43	43.57	22.40	50.18
Cr	6.89	19.71	18.58	6.05	10.99	12.03	14.50	15.43
Fe	8.67	26.04	23.84	3.86	8.89	28.83	6.32	17.14
Si	-	-	0.23	-	0.09	0.38	0.03	0.28
Ni	1.55	2.69	1.45	0.50	0.48	1.72	0.85	1.92
Ce	-	-	0.07	-	-	0.24	0.15	0.33

This elemental partitioning, confirmed by Table 4, is central to understanding the reinforcement mechanism. The enrichment of Ce at the interface of W-rich phases (Figure 4b) further supports its role in modifying local kinetics, promoting WC decomposition and grain refinement. While minor porosity is observed (Figure 4a,b), attributed to trapped gaseous reaction products (CO/CO_2) under rapid solidification, the primary focus and significance of Table 4 lie in its definitive demonstration of how CeO_2 actively regulates solute distribution to form reinforcing silicide and carbide phases, which is the fundamental objective of this study.

3.3. Microhardness

Figure 6 demonstrates the microhardness distribution characteristics of the coatings with different CeO_2 additions. The microhardness of the coatings was measured using a Vickers indenter with a 0.3 kgf load, producing indentations with a diagonal length in the range of 20–30 μm. This method, rather than a bulk hardness test, was selected specifically to evaluate the localized mechanical properties across the coating's cross-section, which consists of a composite microstructure with multiple phases of differing hardness. From Figure 5a, it can be concluded that the average value of microhardness of the 0.4 wt.% CeO_2 coating is 1107.62 $HV_{0.3}$, which is 4.15% higher than that of the coating of the 0.2 wt.% CeO_2 group of 1063.446 $HV_{0.3}$, and 12.43% higher than that of the coating of the 0.6 wt.% CeO_2 group of 985.114 $HV_{0.3}$, and the microhardness of all three coatings' hardness averages were significantly higher than that of the 735.803 $HV_{0.3}$ substrate. From Figure 6b, it can be seen that the fluctuation of the coating microhardness values in the 0.2 wt.% CeO_2 group is attributed to the fact that the amount of CeO_2 added is too small to make the WC particles and their decomposition products diffuse evenly. On the other hand, the hardness distribution of the coatings is relatively uniform after increasing the CeO_2 content, where 0.4 wt.% CeO_2 addition corresponds to the peak hardness value. According to the above XRD analysis results, Fe_6W_6C and Co_6W_6C phases were precipitated from the CeO_2-added coating. As high-hardness hard phases, their formation significantly enhanced the microhardness of the coating [31,32]. Meanwhile, the grain refinement and diffuse distribution effect of the coating organization are also important reasons for the enhanced microhardness. In addition, the decomposed WC particles show a uniform diffuse distribution in the matrix, which further contributes to the improvement of microhardness as a reinforcing skeleton. However, the non-equilibrium

decomposition of excess CeO_2 by adsorption on the surface of WC particles inhibits the precipitation of silicide hard phases, and at the same time, it is easy to form enriched impurity phases at the bottom of the coating due to the high-density property, which ultimately leads to a decrease in microhardness.

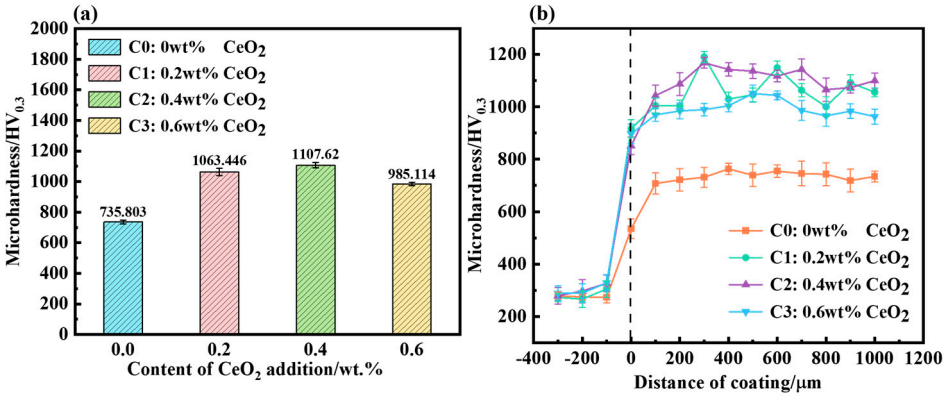


Figure 6. The microhardness of coatings with different levels of CeO_2 addition is as follows: (**a**) average microhardness; (**b**) microhardness distribution.

3.4. Wear Resistance

Figure 7 presents the friction coefficient and wear mass loss of the coatings with varying CeO_2 contents. As shown in Figure 6a, the oscillation amplitude of the friction coefficient curves decreases markedly as the CeO_2 content increases from 0 wt.% to 0.6 wt.%, indicating a progressive stabilization of the friction process. The initial fluctuations in the friction curves, which are most pronounced for the CeO_2—free coating, can be attributed to several interrelated mechanisms characteristic of the running—in period of sliding contact. First, at the onset of sliding, the real contact area between the coating and the counter ball is extremely small. As sliding proceeds, the contacting asperities undergo plastic deformation, fracture, or shearing, generating wear debris of various sizes. This transient asperity interaction leads to substantial friction fluctuations until a smoother steady—state contact condition is established. Second, the wear debris—commonly referred to as the "third body"—detached from both the coating and the counter ball accumulates at the sliding interface. During this running-in stage, the composition, thickness, and distribution of the debris layer are unstable, and its dynamic role (acting either as a lubricant or as an abrasive) directly contributes to the oscillation of the friction coefficient. Third, the real contact area gradually increases with continued sliding, evolving from a very small initial value toward a steady-state value. This transient increase, accompanied by changes in frictional heating and material transfer, further promotes initial frictional instability. The addition of CeO_2 significantly reduces both the magnitude and duration of these initial fluctuations, indicating that CeO_2 facilitates a more rapid transition to stable sliding, likely by promoting the formation of a uniform, protective debris layer and refining the microstructure, as discussed earlier [33,34].

In the present CeO_2 modified coatings, the difference in the amplitude and duration of these initial fluctuations is closely related to the influence of CeO_2 content on microstructural homogeneity. A more uniform microstructure, which is promoted by an optimal CeO_2 addition (0.4 wt.%), facilitates a smoother initial wear process and enables the more rapid formation of a stable, protective debris layer [35,36]. As shown in Figure 8, EDS elemental mapping of the worn surface of the C2 coating (0.4 wt.% CeO_2) reveals pronounced oxygen enrichment, along with localized accumulations of Co, Si, Fe, W, and Cr. Under the synergistic effect of frictional heat and shear stress, elements such as Co, Cr, W, and Si—homogeneously distributed within the coating—undergo oxidation, giving

rise to high-temperature-stable composite oxides enriched with these constituents. These oxides are dynamically generated and continuously replenished at the sliding interface, thereby forming a self-sustaining lubricating film. Consequently, coatings with higher CeO_2 content exhibit more rapid stabilization and reduced oscillation in their friction curves, underscoring the beneficial role of CeO_2 in refining the microstructure and enhancing interfacial stability during sliding. Consequently, the friction curves of coatings with higher CeO_2 contents exhibit quicker stabilization and smaller oscillations, reflecting the beneficial effect of CeO_2 in refining the microstructure and improving the interfacial response during sliding.

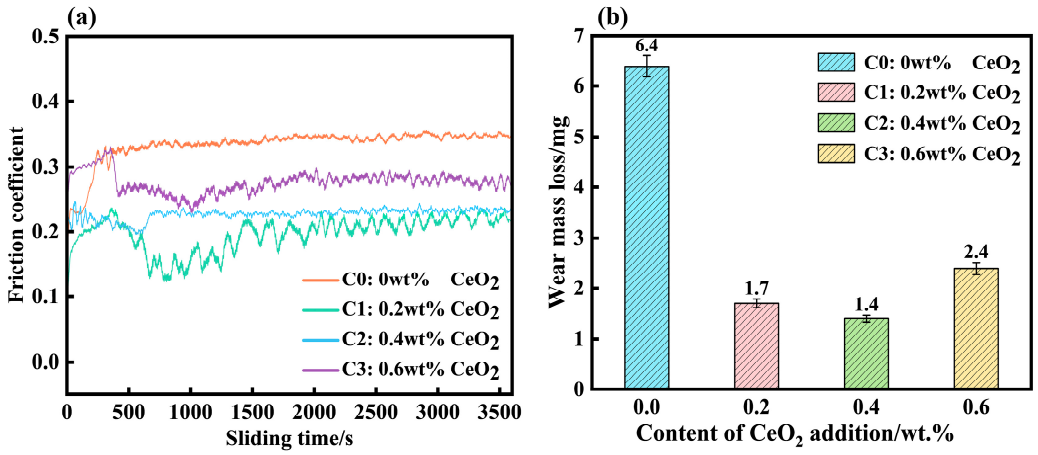


Figure 7. Wear test results with different CeO_2 content: (**a**) friction coefficient and (**b**) wear mass loss.

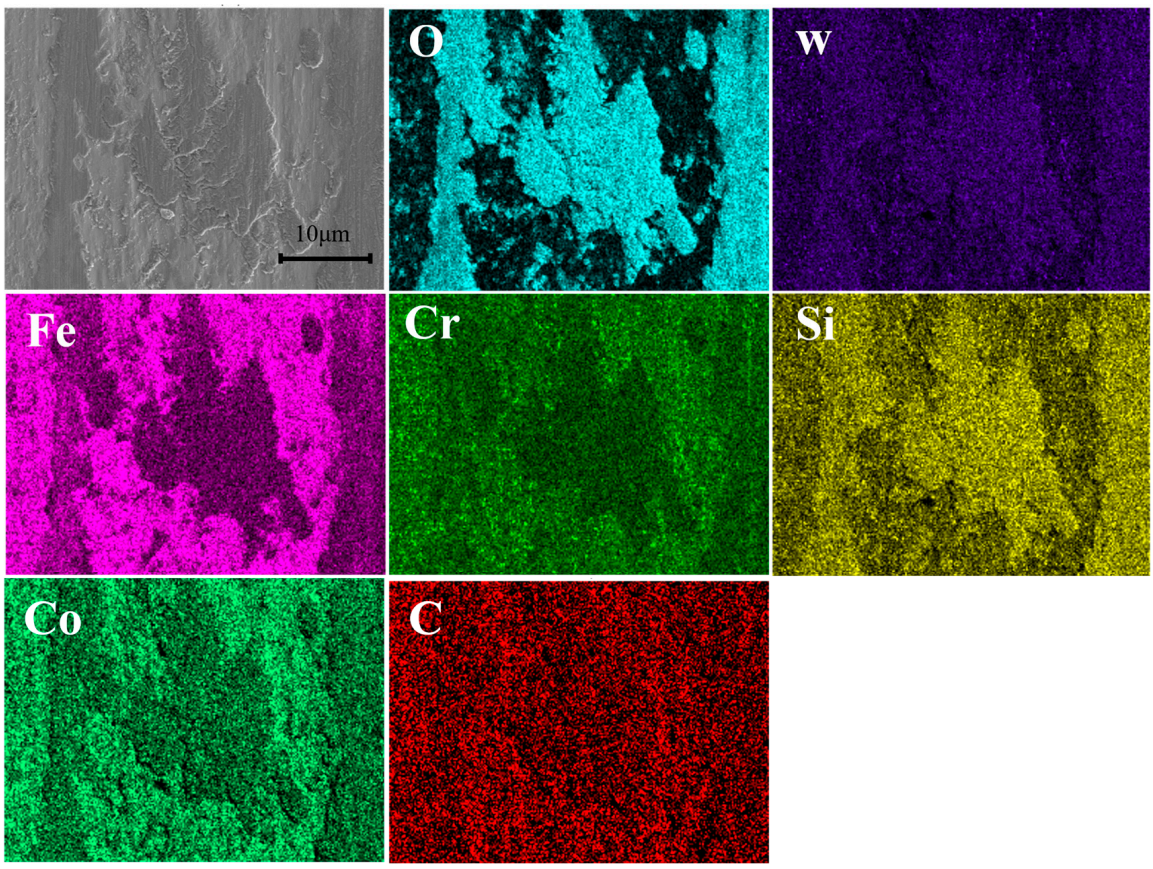


Figure 8. EDS maps of C2 (0.4 wt.%CeO_2) coating.

Quantitative analysis revealed that the average friction coefficient of the unadded coating was 0.35, whereas the coefficient values of the coatings with 0.2 wt.%, 0.4 wt.%, and 0.6 wt.% CeO_2 were 0.21, 0.23, and 0.27, respectively. Although the 0.4 wt.% CeO_2 coating (C2) exhibited the most stable friction curve, its average friction coefficient (0.23) was slightly higher than that of the 0.2 wt.% CeO_2 coating (C1). This difference can be attributed to the microstructural characteristics of the two coatings. In the C1 coating, partially melted WC particles are relatively loosely bonded to the matrix; during sliding, these particles easily detach and act as third-body abrasives, reducing the real contact area and consequently lowering the friction coefficient. In contrast, the C2 coating, benefiting from an optimal CeO_2 addition, possesses a more uniform and denser microstructure, wherein the hard carbides are well-integrated with the matrix and resistant to detachment. It should be emphasized that the friction coefficient alone is not a direct indicator of wear resistance; a lower friction coefficient does not necessarily imply superior wear resistance, as it can be significantly influenced by surface debris, transfer layers, or third-body abrasion. Therefore, a comprehensive evaluation of wear performance requires additional analyses of wear mass loss, three-dimensional surface topography, and worn surface morphology, which are presented and discussed in the following content.

The wear loss data in Figure 7b shows that the wear loss of all coatings is significantly lower than the wear loss of the substrate, with the highest loss of 6.4 mg for the unmodified coating. among them, the 0.4 wt.% CeO_2 coating presents the lowest weight loss of 1.4 mg, which is 78.1% lower than that of the unmodified coating. This phenomenon is attributed to the fact that CeO_2 forms a three-dimensional hard skeleton network by catalyzing the synthesis of carbon/silicide reinforced phases (Cr_3C_2, WSi_2), which can effectively take up frictional loads and inhibit plastic deformation. However, when the CeO_2 addition was increased to 0.6 wt.%, the weight loss increased by 71.4% compared to that of the sample with 0.4 wt.% CeO_2 addition, which implies that excessive CeO_2 triggered the supersaturation of the melt pool composition and inhibited the precipitation of reinforcing phases, leading to the elevation of the ratio of substable carbon-deficient phases (Co_6W_6C), the load-bearing capacity of the coating is weakened.

By analyzing the three-dimensional morphology of the Stellite6/WC composite coatings modified with different CeO_2 contents, as shown in Figure 9, significant wear property differences can be observed. The unmodified C0 coating shows the widest wear track with a maximum width of 1660 μm. With the addition of CeO_2, the wear track width of the composite coatings shows a significant decrease, among which the C2 coating shows the most excellent wear resistance, with the wear track width reduced to 1320 μm, and the wear surface is relatively flat, with only a small amount of micro-plow furrow phenomenon observed. It is worth noting that when the CeO_2 addition exceeded 0.4 wt.%, the wear track width showed an increasing trend, indicating that the excessive addition would lead to a decrease in wear resistance. Nevertheless, the wear track widths of all CeO_2-modified coatings were significantly smaller than those of unmodified C0 coatings. Further analysis of the wear depth data reveals that the trend is highly consistent with the wear width results, which fully confirms that the unmodified coatings suffered more severe surface damage in the sliding wear tests. These morphological features are consistent with the wear rate test results obtained in the previous period, which provide an important experimental basis for the study of the wear resistance mechanism of CeO_2-modified coatings.

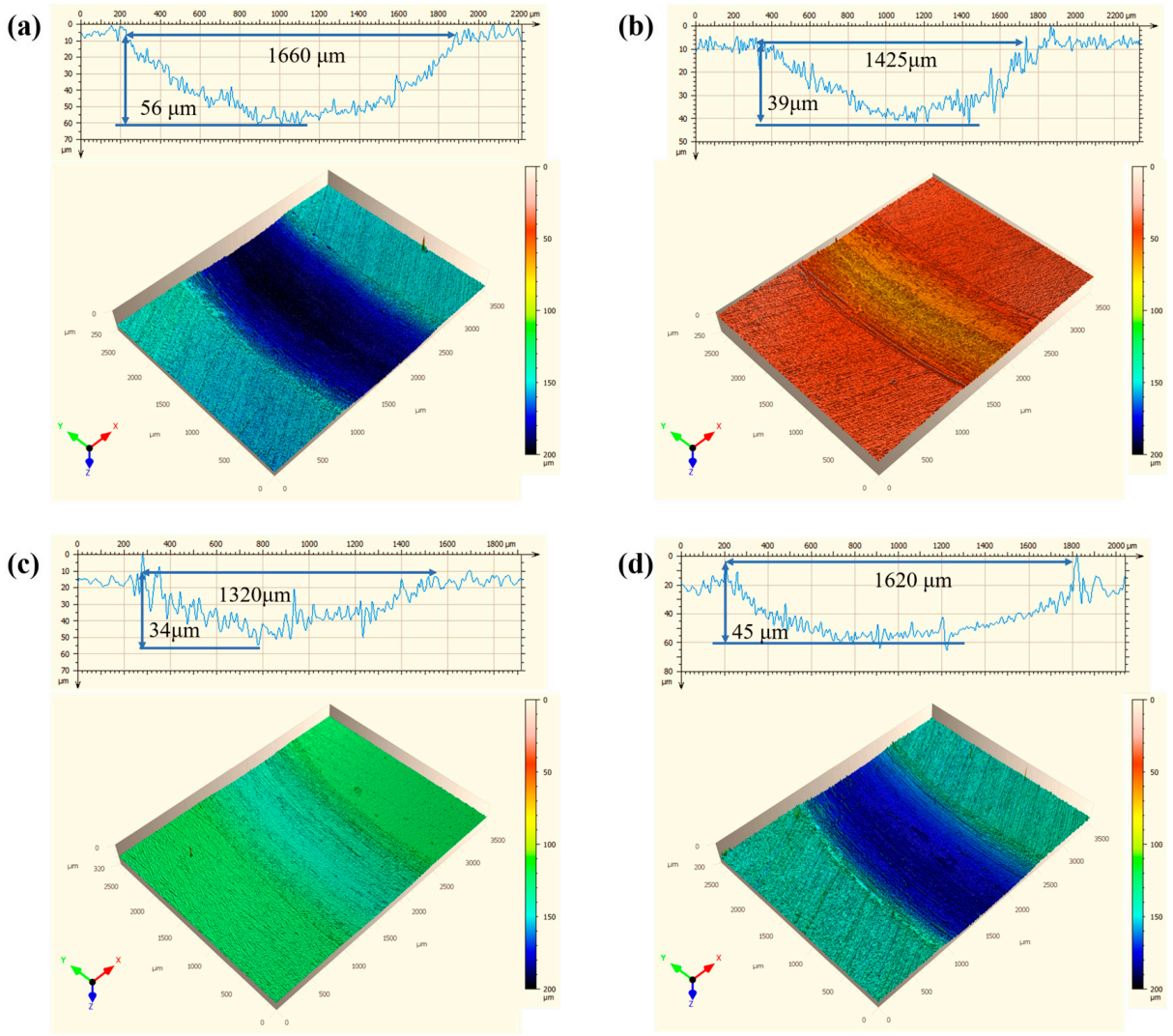


Figure 9. 3D image of coating wear marks. (**a**) C0:0 wt.% CeO_2; (**b**) C1:0.2 wt.% CeO_2; (**c**) C2:0.4 wt.% CeO_2; (**d**) C3:0.6 wt.% CeO_2.

The wear surface morphology of the coatings with different CeO_2 contents is shown in Figure 10. A large amount of debris, as well as detachment pits, can be observed in the C0 coating. The amount of debris is greatly reduced in the C1 coating, but some detachment pits still exist. In the C2 coating, there is almost no debris and no obvious detachment pits, and a large amount of debris appears again in the C3 coating. The wear morphology of the C0~C3 sprayed layers shows typical adhesive wear and abrasive wear characteristics. Among them, C0 coating due to the uneven distribution of W-rich phase, the heating of the contact interface during friction causes localized regional welding, leading to adhesion junctions during relative motion of the friction interface. the adhesion point shear coating in the softer part of the coating, resulting in the coating tear and the formation of a large area of the adhesive layer, accompanied by the migration of the adhesive layer buildup and the eventual shedding of the formation of debris; secondly, the WC particles shed during friction act as third-body abrasive particles to initiate secondary abrasive wear, leading to the formation of furrows and reducing the wear resistance of the coating. It is noteworthy that no significant adhesive wear debris appeared on the surfaces of C1~C3 layers, which was attributed to the dispersed carbide skeleton that inhibited adhesive damage by hindering dislocation motion and resisted abrasive plowing by virtue of its high hardness. In C2, the area covered by the adhesive layer was significantly reduced,

and the smooth area was enlarged. The mechanism is that the presence of the carbide hard phase enhances the overall microhardness, resulting in the strength of the adhesive junction being lower than the strength of the coating's localized area, and the fracture behavior is concentrated at the adhesive interface rather than inside the coating, thus avoiding the accumulation of adhesive layer and improving the wear resistance [37,38]. The surface of the sprayed layer C3 is smooth without traces of adhesive tearing, but there is obvious shedding debris. This is due to the fact that excessive addition of CeO_2 leads to precipitation of the W-rich phase in the form of coarse branches; this kind of brittle dendrites and the bonding phase interface bond strength weakened, and under the action of frictional shear stress, spalling occurs, which ultimately leads to a significant reduction in the wear resistance of the coating.

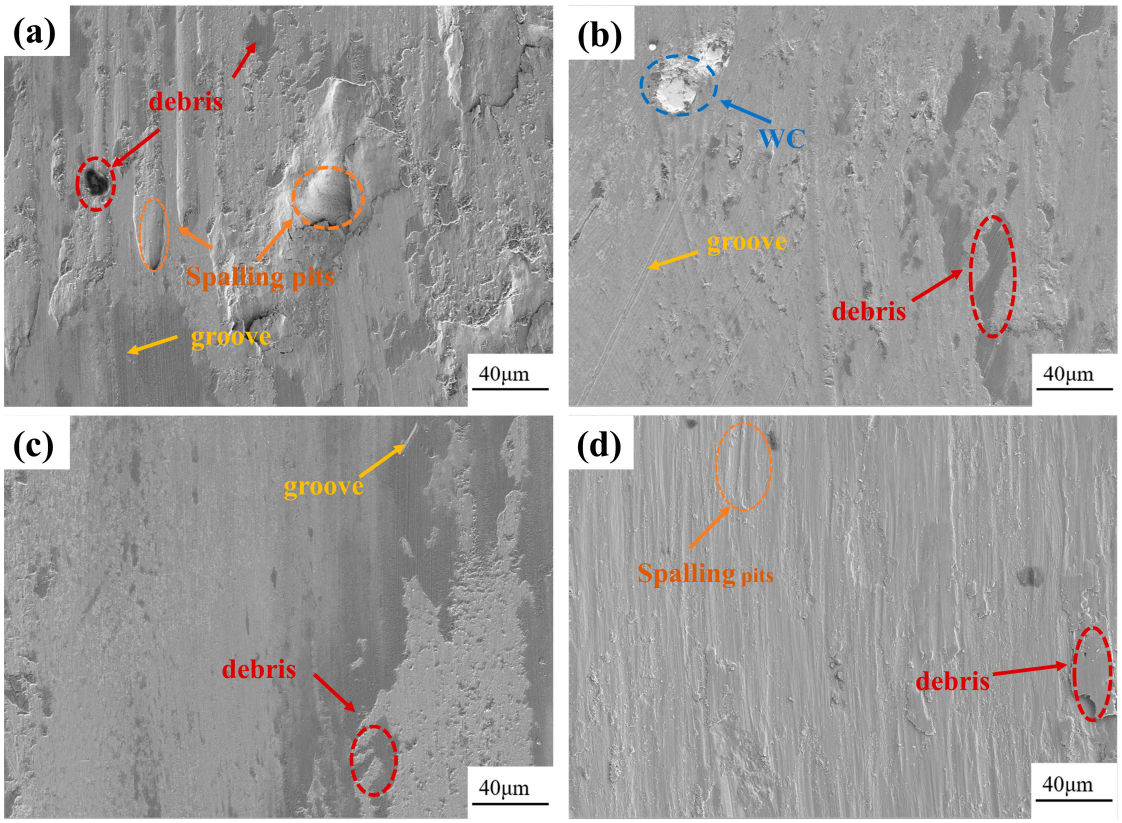


Figure 10. SEM images of coated wear surfaces. (**a**) C0:0 wt.% CeO_2; (**b**) C1:0.2 wt.% CeO_2; (**c**) C2:0.4 wt.% CeO_2; (**d**) C3:0.6 wt.% CeO_2.

4. Conclusions

In this study, Co-based tungsten carbide sprayed layer was prepared on the surface of 45 steel by the plasma spraying technique. The effect of CeO_2 content on the organization and properties of the coating was investigated. The main conclusions are as follows:

(1) The addition of CeO_2 refines the microstructure and alters the morphology of the reinforcing phases. Specifically, at 0.2 wt.% CeO_2, the originally spherical WC particles begin to transform into a maple-leaf shape, and the precipitation of secondary carbides and silicides (W_5Si_3, Si_2W) is promoted, leading to a more uniform distribution. At 0.4 wt.% CeO_2, this refinement reaches an optimum: WC particles become finely and uniformly dispersed, secondary silicides are maximally precipitated, and a continuous "three-dimensional hard skeleton network" is formed. However, when the CeO_2 content increases to 0.6 wt.%, the WC particles evolve into irregular dendritic forms, and further precipitation of silicides is suppressed, indicating that excessive CeO_2 disrupts the optimal microstructure.

(2) The addition of CeO_2 improves the microhardness of the coating by promoting WC decomposition and secondary phase precipitation, thereby converting the strengthening mechanism from solid-solution strengthening alone to a combination of solid-solution strengthening and dispersion/precipitation strengthening. Specifically, microhardness increases from 735.8 $HV_{0.3}$ (0 wt.%) to 1063.4 $HV_{0.3}$ at 0.2 wt.% CeO_2, reaches a peak of 1107.6 $HV_{0.3}$ at 0.4 wt.% (a 50.5% improvement), and then decreases to 985.1 $HV_{0.3}$ at 0.6 wt.%. Thus, 0.4 wt.% CeO_2 yields the highest microhardness among all compositions.

(3) With increasing CeO_2 content, the wear resistance of the coating first increases and then decreases, reaching its optimum at 0.4 wt.% CeO_2 addition. The coating with 0.2 wt.% CeO_2 shows a notable improvement in wear resistance (mass loss of 1.7 mg, a 73.4% reduction compared to the unmodified coating). The 0.4 wt.% CeO_2 coating exhibits the lowest wear mass loss (1.4 mg)—a reduction of 78.1% compared to the unmodified coating—which represents the fundamental quantitative evidence of its superior wear resistance. This is corroborated by the most stable friction process, as reflected in the steady coefficient of friction curve with minimal fluctuations. In contrast, the 0.6 wt.% CeO_2 coating shows a deterioration in wear resistance (mass loss of 2.4 mg, a 62.5% reduction), indicating that excessive CeO_2 is detrimental to tribological performance. Post-wear characterization further confirms that the 0.4 wt.% CeO_2 coating exhibits the shallowest and narrowest wear track, with a wear morphology dominated by mild abrasion rather than severe delamination or debris accumulation. Therefore, among the three concentrations tested, the 0.4 wt.% CeO_2 coating demonstrates the optimal tribological performance.

Author Contributions: M.W.: Data collection, Writing—original draft; Z.M.: Supervision, funding acquisition, Writing—review & editing; Y.C.: Investigation, Data collection, Validation; R.L.: Conceptualization, Methodology, Validation, Investigation; J.D.: Methodology, Validation, Investigation, Data curation; D.F.: Conceptualization, Methodology, Validation; Z.H.: Methodology, Validation, Investigation, Data curation. All authors have read and agreed to the published version of the manuscript.

Funding: This research received no external funding.

Institutional Review Board Statement: Not applicable.

Informed Consent Statement: Not applicable.

Data Availability Statement: The raw data supporting the conclusions of this article will be made available by the authors on request.

Conflicts of Interest: The authors declare no conflicts of interest.

References

1. Li, Q.; Xiao, K.; Lu, Z.; Shi, Y.; Lin, W.; Zhang, S. Mechanism of laser carbonitriding enhancing the wear resistance of 45# steel. *Mater. Today Commun.* **2024**, *38*, 108327. [CrossRef]
2. Ma, Q.; Zhang, H.; Lv, Y.; Song, C.; Guo, N.; Xiao, G.; Zhao, W. Microstructure and properties of $W_{0.5}Ta_{0.3}MoNbVAlTi_{1-x}Zr_x$ high entropy alloy coatings by laser cladding on the surface of 45# steel. *Ceram. Int.* **2023**, *49*, 36416–36428.
3. Liu, Q.-S.; Liu, X.-B.; Wang, G.; Liu, Y.-F.; Meng, Y.; Zhang, S.-H. Effect of Cu content on microstructure evolution and tribological behaviors of Ni60 composite coatings on 45# steel by laser cladding. *Opt. Laser Technol.* **2022**, *156*, 108549. [CrossRef]
4. Liu, H.; Wang, C.; Zhang, X.; Jiang, Y.; Cai, C.; Tang, S. Improving the corrosion resistance and mechanical property of 45 steel surface by laser cladding with Ni60CuMoW alloy powder. *Surf. Coat. Technol.* **2013**, *228*, S296–S300. [CrossRef]
5. Narendra, N.B.; Pavithran, V.; Barat, S.; Ramanathan, P.; Govindarajan, S. High temperature tribological performance of stellite-6 coating deposited on SS304 substrate by HVAF process. *Next Res.* **2026**, *4*, 101221.
6. Baiamonte, L.; Tului, M.; Bartuli, C.; Marini, D.; Marino, A.; Menchetti, F.; Pileggi, R.; Pulci, G.; Marra, F. Tribological and high-temperature mechanical characterization of cold sprayed and PTA-deposited Stellite coatings. *Surf. Coat. Technol.* **2019**, *371*, 322–332. [CrossRef]

7. Kishore, K.; Jaiswal, N.; Prabhakaran, A.; Arora, K.S. Through-thickness microstructure and wear resistance of plasma transferred arc Stellite 6 cladding: Effect of substrate. *CIRP J. Manuf. Sci. Technol.* **2023**, *42*, 24–35. [CrossRef]
8. Xie, Z.; Zhang, C.; Wang, R.; Li, D.; Zhang, Y.; Li, G.; Lu, X. Microstructure and wear resistance of WC/Co-based coating on copper by plasma cladding. *J. Mater. Res. Technol.* **2021**, *15*, 821–833. [CrossRef]
9. Al-Mutairi, S.; Hashmi, M.S.J.; Yilbas, B.S.; Stokes, J. Microstructural characterization of HVOF/plasma thermal spray of micro/nano WC–12%Co powders. *Surf. Coat. Technol.* **2015**, *264*, 175–186. [CrossRef]
10. Özgün, Ö.; Dinler, İ. Production and Characterization of WC-Reinforced Co-Based Superalloy Matrix Composites. *Metall. Mater. Trans. A* **2018**, *49*, 2977–2989. [CrossRef]
11. Zhang, A.; Jiang, L.; Deng, H.; Li, Y.; Liang, H.; Chen, C.; Zhu, Z.; Cao, Z.; Zhang, W. Optimized wear behavior and oxidative strengthening mechanism of a WC reinforced high entropy composite coatings. *J. Mater. Res. Technol.* **2025**, *36*, 6473–6485. [CrossRef]
12. Zheng, Y.; Yang, Z.; Tian, Z.; Chen, J.; Lu, H.; Zhang, K. Sedimentation suppression and precipitation regulation of WC-reinforced particles in plasma arc deposited Ni-based coatings via an alternating magnetic field. *J. Mater. Res. Technol.* **2023**, *25*, 7512–7527.
13. Miao, X.; Wu, M.; Wang, H.; Zhao, Y.; Cui, C.; He, R.; Jie, D. Effects of La content on microstructure and tribological properties of laser clad Ni60/WC/La_2O_3 composite coatings on Cr12MoV. *J. Mater. Res. Technol.* **2024**, *29*, 2667–2678. [CrossRef]
14. Xiao, D.H.; He, Y.H.; Song, M.; Lin, N.; Zhang, R.F. Y_2O_3- and NbC-doped ultrafine WC–10Co alloys by low pressure sintering. *Int. J. Refract. Met. Hard Mater.* **2010**, *28*, 407–411.
15. Hou, Q.; Huang, Z.; Gao, J. Effects of Y2O3 on the microstructure and wear resistance of cobalt-based alloy coatings deposited by plasma transferred arc process. *Rare Met.* **2007**, *26*, 103–109.
16. Zhang, Z.; Yang, F.; Zhang, H.; Zhang, T.; Wang, H.; Xu, Y.; Ma, Q. Influence of CeO_2 addition on forming quality and microstructure of TiC_x-reinforced $CrTi_4$-based laser cladding composite coating. *Mater. Charact.* **2021**, *171*, 110732.
17. Zhu, R.; Zhu, C.; Wu, S.; Wan, X.; Li, G. Effect of CeO_2 on microstructure and properties of Ni–Co-based coatings. *J. Mater. Res. Technol.* **2023**, *26*, 7329–7339.
18. Xie, G.; Zhang, B.; Liu, H.; Xin, D.; Cai, Y.; Mu, W. Simultaneous enhancement of hardness and toughness of nano-CeO_2 modified multi-scale WC-10Co-4Cr coating via HVOF. *Mater. Lett.* **2025**, *390*, 138418.
19. Zhang, L.; Sun, D.; Yu, H. Characteristics of plasma cladding Fe-based alloy coatings with rare earth metal elements. *Mater. Sci. Eng. A* **2007**, *452–453*, 619–624. [CrossRef]
20. He, W.; Tan, D.; Kuang, H.; Li, Y.; Yang, X.; Zhu, H. Effect of yttrium barrier on the preparation of precursor powders of WC-Co cemented carbide and properties of sintered bulk. *J. Alloys Compd.* **2018**, *742*, 702–711.
21. Ouyang, S.; Qiu, L.; Wang, C.; Wu, D.; Yang, Q.; Chen, L.; Ye, Y.; Chen, H. Influence of Ru content on mechanical, corrosion and oxidation behaviors of WC-15Co cemented carbides. *Ceram. Int.* **2023**, *49*, 23950–23957. [CrossRef]
22. Pu, J.; Sun, Y.-B.; Wu, L.; He, P.; Long, W.-M. Effect of CeO_2 Content on Microstructure and Properties of Ni-Based Tungsten Carbide Layer by Plasma Arc Cladding. *Coatings* **2022**, *12*, 342. [CrossRef]
23. Li, Y.; Liu, D.; Ning, L.; Dang, X.; Dong, J.; Liang, R.; Geng, Y.; Cheng, F.; Zhang, F.; Qu, K.; et al. Wear resistance enhancement of laser cladded Stellite 6 coatings by incorporating micron-nano dual-scale WC reinforcement. *Surf. Coat. Technol.* **2026**, *521*, 133073. [CrossRef]
24. He, L.; Tan, Y.; Wang, X.; Xu, T.; Hong, X. Microstructure and wear properties of Al_2O_3-CeO_2/Ni-base alloy composite coatings on aluminum alloys by plasma spray. *Appl. Surf. Sci.* **2014**, *314*, 760–767.
25. Zhang, Z.; Lu, X.; Luo, J. Tribological properties of rare earth oxide added Cr_3C_2–NiCr coatings. *Appl. Surf. Sci.* **2007**, *253*, 4377–4385. [CrossRef]
26. Chauhan, H.R.; Saladi, S.; Variya, S.; Solanki, A.; Tailor, S.; Sooraj, K.P.; Ranjan, M.; Joshi, S. Role of micro- and nano-CeO_2 reinforcements on characteristics and tribological performance of HVOF sprayed Cr_3C_2-NiCr coatings. *Surf. Coat. Technol.* **2023**, *467*, 129684. [CrossRef]
27. Tian, Y.S.; Chen, C.Z.; Chen, L.X.; Huo, Q.H. Effect of RE oxides on the microstructure of the coatings fabricated on titanium alloys by laser alloying technique. *Scr. Mater.* **2006**, *54*, 847–852. [CrossRef]
28. Zhang, Z.; Wang, Z.; Liang, B.; Dong, H.B.; Hainsworth, S.V. Effect of CeO_2 on the microstructure and wear behavior of thermal spray welded NiCrWRE coatings. *Wear* **2007**, *262*, 562–567.
29. Quazi, M.M.; Fazal, M.A.; Haseeb, A.S.M.A.; Yusof, F.; Masjuki, H.H.; Arslan, A. Effect of rare earth elements and their oxides on tribo-mechanical performance of laser claddings: A review. *J. Rare Earths* **2016**, *34*, 549–564. [CrossRef]
30. Jiang, Q.; Tian, Y.; Shu, F.; Zhao, H.; Sun, Y.; He, W.; Xu, B. Strengthening mechanism and properties of Co–WC composite coatings deposited by plasma-transferred arc welding. *Micro Nano Lett.* **2019**, *14*, 717–720.
31. Ghadami, F.; Ghadami, S.; Davoudabadi, M.A. Sliding Wear Behavior of the Nanoceria-Doped AlCrFeCoNi High-Entropy Alloy Coatings Deposited by Air Plasma Spraying Technique. *J. Therm. Spray Technol.* **2022**, *31*, 1263–1275. [CrossRef]
32. Doleker, K.M.; Ozgurluk, Y.; Kahraman, Y.; Karaoglanli, A.C. Oxidation and hot corrosion resistance of HVOF/EB-PVD thermal barrier coating system. *Surf. Coat. Technol.* **2021**, *409*, 126862. [CrossRef]

33. Mahade, S.; Mulone, A.; Björklund, S.; Klement, U.; Joshi, S. Investigating load-dependent wear behavior and degradation mechanisms in Cr_3C_2–NiCr coatings deposited by HVAF and HVOF. *J. Mater. Res. Technol.* **2021**, *15*, 4595–4609. [CrossRef]
34. Henke, H.; Adam, D.; Köhler, A.; Heimann, R.B. Development and testing of HVOF-sprayed tungsten carbide coatings applied to moulds for concrete roof tiles. *Wear* **2004**, *256*, 81–87. [CrossRef]
35. Saladi, S.; Menghani, J.; Prakash, S. Effect of CeO_2 on Cyclic Hot-Corrosion Behavior of Detonation-Gun Sprayed Cr_3C_2-NiCr Coatings on Ni-Based Superalloy. *J. Mater. Eng. Perform.* **2015**, *24*, 1379–1389.
36. Du, J.; Li, F.; Li, Y.; Lu, H.; Qi, X.; Yang, B.; Li, C.; Yu, P.; Wang, J.; Gao, L. The influence of nano-CeO_2 on tribological properties and microstructure evolution of Cr_3C_2-NiCrCoMo composite coatings at high temperature. *Surf. Coat. Technol.* **2021**, *428*, 127913. [CrossRef]
37. Bolelli, G.; Berger, L.M.; Börner, T.; Koivuluoto, H.; Matikainen, V.; Lusvarghi, L.; Lyphout, C.; Markocsan, N.; Nylén, P.; Sassatelli, P.; et al. Sliding and abrasive wear behaviour of HVOF- and HVAF-sprayed Cr_3C_2–NiCr hardmetal coatings. *Wear* **2016**, *358–359*, 32–50.
38. Zhang, Z.; Liang, B.; Guo, H. The Effect of CeO_2 Addition on the Microstructure and Properties of Ni-Based Flame-Spray Coatings. *J. Therm. Spray Technol.* **2014**, *23*, 725–731.

Disclaimer/Publisher's Note: The statements, opinions and data contained in all publications are solely those of the individual author(s) and contributor(s) and not of MDPI and/or the editor(s). MDPI and/or the editor(s) disclaim responsibility for any injury to people or property resulting from any ideas, methods, instructions or products referred to in the content.